Quantum paraelectricity and structural phase transitions in strontium titanate beyond density-functional theory

Supplemental Material

Carla Verdi,[1, *] Luigi Ranalli,[1] Cesare Franchini,[1, 2] and Georg Kresse[1, 3]

[1] *University of Vienna, Faculty of Physics, Computational Materials Physics, Kolingasse 14-16, 1090 Vienna, Austria*[†]
[2] *Department of Physics and Astronomy, Alma Mater Studiorum - Università di Bologna, Bologna, Italy*
[3] *VASP Software GmbH, Sensengasse 8, 1090 Vienna, Austria*

DETAILS OF FIRST-PRINCIPLES CALCULATIONS

Here we provide additional details of our density-functional theory (DFT) calculations and the random-phase approximation (RPA). As specified in the main text, DFT calculations were performed using VASP [1, 2], adopting the PBEsol exchange-correlation functional [3], as well as the rSCAN meta-GGA [4] and the HSE06 hybrid functional [5, 6]. For the calculations using PBEsol we employed the standard projector augmented wave (PAW) potentials for O and Sr, with the Sr 4s and 4p semicore states treated as valence states, and the GW PAW potential for Ti with the 3s and 3p semicore states included in the valence. For all other calculations we employed the GW potentials for each element (note that in the case of oxygen, the O_GW_new potential which possesses d-projectors was used). Tight convergence criteria were imposed in all DFT calculations by setting the plane-wave cutoff to 700 eV, including a small Pulay stress correction of -2.7 to -4.7 kbar due to the finite plane-wave basis set size. We used a $8 \times 8 \times 8$ Monkhorst-Pack k-mesh to sample the Brillouin zone of the primitive cubic cell consisting of 5 atoms (space group $Pm\bar{3}m$), while a $6 \times 6 \times 6$ k-mesh ensures similar convergence for the primitive tetragonal cell containing 10 atoms (space group $I4/mcm$). The conventional cells of the cubic and tetragonal structures are shown in Fig. S1. Structural optimizations were performed until the forces were smaller than 0.2 meV/Å. Spin-orbit coupling was neglected, as it was found to have no impact on the phonon instabilities and the associated potential energy surfaces.

The RPA calculations were performed using the low-scaling algorithm of Ref. [7]. The plane-wave cutoff was set to 650 eV, while the energy cutoff for the response function was 433 eV. To facilitate smoother convergence of the RPA correlation energies, we employed a cosine window function to smoothly cut off the contributions from the largest 20% wave vectors components in the response function. The number of imaginary time and frequency grid points for calculating the independent-particle polarizability was set to 12. Due to the large computational cost of RPA calculations and especially RPA forces, the Brillouin zone was sampled using a $6 \times 6 \times 6$ k-grid for the primitive cubic cell and a $4 \times 4 \times 4$
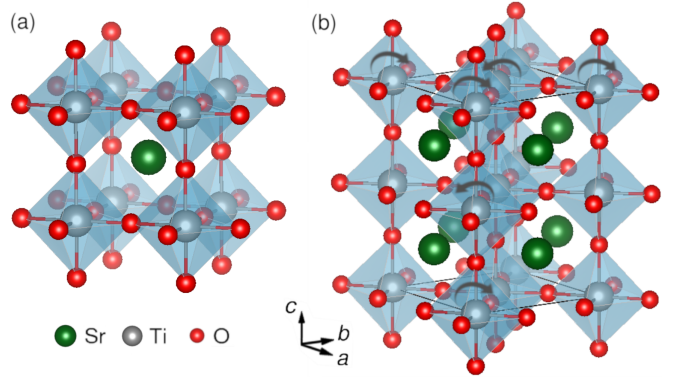

FIG. S1. Ball-and-stick model of the (a) cubic and (b) tetragonal conventional unit cell of strontium titanate. The gray arrows in (b) indicate AFD rotations of the oxygen octahedra.

k-grid for the tetragonal cell. These settings yield a relative energy accuracy of better than 0.2 meV/atom. Since the RPA correlation energies converge very slowly with the energy cutoff, an extrapolation procedure to the infinite basis set limit is usually employed [8]. In this work, the equilibrium RPA volumes were calculated using the extrapolated energies following this procedure, by fitting energy versus volume data with a Birch-Murnaghan equation of state. As shown in Fig. S2, using the non-extrapolated energies would result in an overestimation of the optimized volumes by 0.4%. In order to train our RPA-based MLFF, however, the non-extrapolated energies must be considered. This ensures consistency between energies and forces. To account for the infinite basis set limit, a small pressure of 8 kbar was then applied to the system, restoring the correct equilibrium volumes.

MLFF TRAINING AND VALIDATION

The details of the kernel-based MLFF model adopted and its implementation can be found in Refs. [9, 10]. The model follows the Gaussian approximation potential (GAP) approach [11], where each atomic energy contribution is expressed as a linear combination of kernel functions. The kernel measures the similarity between local
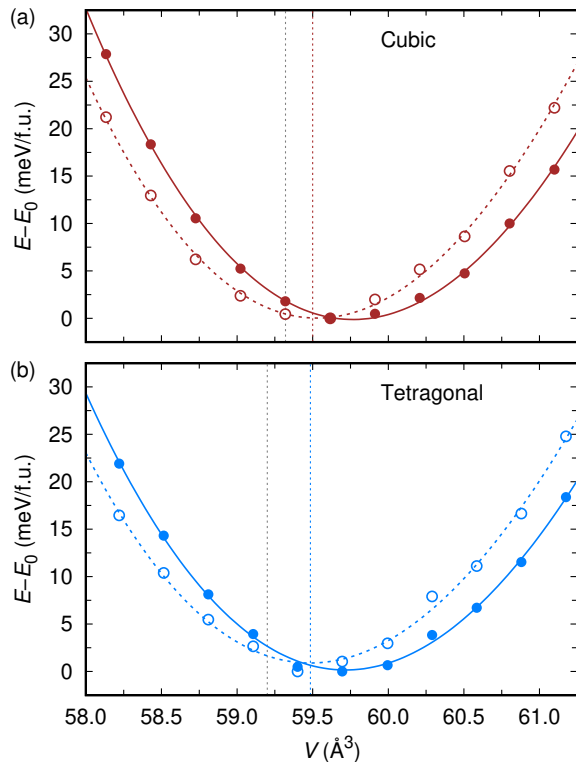
FIG. S2. Energy versus volume curves for (a) cubic and (b) tetragonal SrTiO$_3$ calculated using the RPA. The filled circles are the non-extrapolated energies, while the empty circles are the extrapolated ones. The solid and dashed lines are the respective fits using the Birch-Murnaghan equation of state. The vertical lines indicate the experimental (gray) and RPA (colored) equilibrium volumes. The energies are given per formula unit (f.u.) and are shifted to the minimum values. In (b) the volume refers to the pseudo-cubic unit cell.

atomic environments. Here it was taken as the polynomial kernel calculated from the dot product of normalized descriptors vectors followed by an exponentiation by $\zeta = 4$. Similarly to Ref. [12], we used supercells containing 320 atoms and a $2 \times 2 \times 2$ k-mesh in order to train the initial MLFF based on PBEsol data. For the on-the-fly training, the molecular dynamics (MD) simulations were performed in two steps. First, starting from a $4 \times 4 \times 4$ supercell of the cubic structure (320 atoms), we gradually heated the system from a temperature of 150 K to 350 K in 150 ps, letting the volume fluctuate at ambient pressure. Then, we further trained the MLFF by starting from a tetragonal structure and heating it from 10 K to 150 K for another 150 ps. First-principles calculations are only performed for a small fraction of the MD steps, here 626 in total. These structures were selected on the basis of the predicted Bayesian error in the forces, which measures the uncertainty of the MLFF predictions: when this error is large, first-principles calculations are performed, and the results added to the training dataset. In

this way, a robust training dataset is efficiently created. To represent the local environment around each atom, we used separable two- and three-body descriptors [10] calculated using a Gaussian broadening of 0.2 Å for the atomic distribution function and a cutoff radius of 6 Å. We found the use of a relatively small broadening to be necessary to accurately describe the soft phonon modes. Up to 22 spherical Bessel functions (for the angular quantum number $l = 0$) and Legendre polynomials of order up to $l = 4$ were employed to expand the atomic distributions. Energies, forces and stress components were weighted equally when solving the Bayesian regression problem to determine the fitting coefficients.

To train the rSCAN and RPA-derived MLFFs we used a Δ-learning procedure [13]. A new set of training structures was generated on the fly during MD simulations with the same setup as for the original training set but using smaller cells. 100 training structures containing 40 atoms (10 atoms) were collected, and for each structure we computed the difference Δ between the rSCAN and PBEsol (RPA and PBEsol) energies and forces. An MLFF, denoted MLFF-Δ, was fitted to reproduce such differences for both rSCAN and the RPA, using descriptors with a lower spatial resolution of 0.5 Å and 8 radial basis functions. Then, the PBEsol data for all the 626 structures in the original training set were 'corrected' by adding the differences predicted by MLFF-Δ, both at the rSCAN and RPA level. This step allows to finally train an rSCAN and RPA-derived MLFF using the updated training data. Note that in the case of rSCAN the differences in the stress tensors were also calculated, but not for the RPA, and therefore they were not included in the MLFF-Δ fitting in the latter case. Indeed, we tested that the stress tensor could be accurately predicted from the energy and force data alone.

To assess the accuracy of our MLFFs, Fig. S3 shows the comparison between the energies and forces calculated for test datasets directly from AI calculations and using the corresponding MLFFs trained to reproduce PBEsol, rSCAN and the RPA. For PBEsol and rSCAN, the test dataset consists of 150 structures of 320 atoms sampled between 10 and 300 K [panels (a) and (b)]. As reported in the main text, the RMSEs in the energies and forces are, respectively, 0.18 meV/atom and 0.037 eV/Å for PBEsol, and 0.22 meV/atom and 0.040 eV/Å for rSCAN. For the RPA, we used a test set of 25 structures of 10 atoms each sampled at temperatures up to 350 K. PBEsol data for the same structures are also reported for comparison [panels (c) and (d)]. The RMSEs in the energies and forces are similar for PBEsol and the RPA, namely 0.71 meV/atom and 0.031 eV/Å (PBEsol), and 0.56 meV/atom and 0.033 eV/Å (RPA). The larger error in the calculated energies per atom as compared to calculations in the larger supercells is due to simple error propagation with respect to the system size [13].

We further tested the accuracy of the MLFFs by com-

puting some key physical properties and comparing them to direct *ab initio* calculations. Namely, from Table SI we see that the structural parameters, AFD and FE mode frequencies, and energy differences between the cubic and tetragonal phase predicted by the MLFFs are all in excellent agreement with the *ab initio* ones. The phonon dispersions computed using rSCAN and the associated MLFF are shown in Fig. S4(b) and (c) for cubic and tetragonal SrTiO₃, respectively. For PBEsol (not shown) we observe a similar level of agreement. Direct RPA calculations yielding the phonon frequencies at the Γ and R point of the cubic Brillouin zone are shown in Fig. S4(a), and are in very good agreement with the prediction from the MLFF-RPA. Finally, the potential energy surfaces (PES) obtained by diplacing the atoms in the tetragonal unit cell along the FE soft modes are reproduced very accurately by the MLFFs (see Fig. 1(a) and (e) in the main text). Fig. S6 and S8 show the agreement for the 2D PES calculated using MLFF-rSCAN and directly using rSCAN.

SSCHA CALCULATIONS

The SSCHA method is based on a quantum variational principle in the free energy F [14]:

$$F_H \leq \mathcal{F}_H[\mathcal{H}] = F_{\mathcal{H}} + \int d\mathbf{R} \left[V(\mathbf{R}) - \mathcal{V}(\mathbf{R}) \right] \rho_{\mathcal{H}}(\mathbf{R}) \quad \text{(S1)}$$

where H is the 'true' Hamiltonian of the system, with potential energy V, and $\mathcal{H}$ is a trial Hamiltonian which is taken to be harmonic with the harmonic potential $\mathcal{V}$. Here we denote with $\mathbf{R}$ the full set of atomic positions of the system, $R_{i,\alpha}$ (bold notation indicates a vector or a tensor, i is an atom index, and Greek symbols indicate Cartesian coordinates), and with $\mathbf{\mathcal{R}}$ the average atomic positions. The quantum probability distribution $\rho_{\mathcal{H}}(\mathbf{R})$ associated to $\mathcal{H}$ depends explicitly on the average atomic positions $\mathbf{\mathcal{R}}$ and on the auxiliary force constants $\mathbf{\Phi}$, $\rho_{\mathbf{\mathcal{R}},\mathbf{\Phi}}$. It has a Gaussian form, allowing the integral in Eq. (S1) to be calculated exactly.

The SSCHA method performs a stochastic minimization of Eq. (S1) as follows. First, starting from the harmonic dynamical matrices and an unperturbed supercell structure, an ensemble of configurations is obtained by randomly displacing all the atoms in the given supercell according to the Gaussian distribution corresponding to the harmonic phonons at a specified temperature. After calculating the energies and forces for each configuration, the anharmonic free energy and its gradient are computed stochastically, and the minimization is performed using a preconditioned gradient descent approach [15]. During the minimization, the average positions of each atom $\mathbf{\mathcal{R}}_i$ as well as the auxiliary force constants matrix $\mathbf{\Phi}$ are updated. By means of importance sampling,

the ensemble of configurations generated with the initial Gaussian distribution is exploited for the stochastic minimization until it is no longer representative of the updated probability distribution [15]. Here we set the threshold for the Kong-Liu effective sample size to 25% of the initial size. A new ensemble is then generated using the updated distribution, and the procedure is repeated until the free energy is minimized. Note that a more efficient evaluation of the stochastic integrals could be performed via the method recently proposed in Ref. [16].

To reach the anharmonic ground state at zero kelvin, we generated 6 ensembles of 1500 configurations each using supercells containing 320 atoms for the cubic structure ($4 \times 4 \times 4$ replica of the 5-atom unit cell) and 270 atoms for the tetragonal structure ($3 \times 3 \times 3$ replica of the 10-atom unit cell). For each subsequent temperature considered (in steps of 25 K), one additional ensemble was sufficient to minimize the free energy when starting from the effective harmonic force constants and atomic positions obtained at the preceding temperature. To accurately compute the free-energy differences between the cubic and tetragonal phase as a function of temperature [see Fig. 3(c) in the main text], we adopted the same 270-atom supercell also for the cubic phase.

The anharmonic phonon frequencies are obtained from the diagonalization of the (mass-scaled) free energy Hessian $\partial^2 F/(\partial \mathcal{R}_{i,\alpha} \mathcal{R}_{j,\beta})$ calculated at the equilibrium configuration. This formally corresponds to the static approximation of the anharmonic SSCHA self-energy [17]. The Hessian of the free energy is given by:

$$\frac{\partial^2 F}{\partial \mathbf{\mathcal{R}} \partial \mathbf{\mathcal{R}}} = \mathbf{\Phi} + \mathbf{\Phi}^{(3)} \mathbf{\Lambda}(0) \left(1 - \mathbf{\Phi}^{(4)} \mathbf{\Lambda}(0) \right)^{-1} \mathbf{\Phi}^{(3)}, \quad \text{(S2)}$$

where $\mathbf{\Phi}^{(3)}$ and $\mathbf{\Phi}^{(4)}$ are the effective SSCHA third- and fourth-order force constants, calculated as stochastic averages using the usual Gaussian distribution $\rho_{\mathbf{\mathcal{R}},\mathbf{\Phi}}$, while $\mathbf{\Lambda}(0)$ is readily obtained from the effective harmonic SSCHA phonons [17]. We found that in the range of temperatures considered, the contribution coming from $\mathbf{\Phi}^{(4)}$ can be safely neglected, as often found in other works [15, 18]. The stochastic calculation of the free energy Hessian requires a larger number of configurations than for the free energy. Converged results were obtained by using 5000 configurations for each temperature (increased to 8000 for the points shown in Fig. 3(d) in the main text). Overall, these settings ensure that the computed anharmonic phonons are accurate within 0.5 meV. As a final assessment of the accuracy of the MLFFs, we performed a SSCHA minimization directly from first principles using the PBEsol exchange-correlation functional and a 40-atom cubic supercell. The resulting anharmonic phonons are in excellent agreement with the ones computed using the MLFF. In particular, the strongly renormalized FE and AFD phonons agree within less than 0.3 meV.

TABLE SI. Structural parameters for cubic and tetragonal SrTiO$_3$, energy differences between the two phases ($\Delta E_{\text{c-t}}$) and AFD and FE phonon instabilities in the cubic phase. θ_z indicates the rotation angle of the octahedra around the z axis in the tetragonal phase. The energy differences and the volumes are reported per formula unit, with $\Delta E_{\text{c-t}}$ calculated at the experimental volumes for the RPA. The results from the MLFFs are compared to the corresponding *ab initio* calculations (MLFF-PS indicates the MLFF trained on PBEsol) and to the experimental data [19, 20]. The values of c/a in parenthesis are results at 0 K after taking into account the effects of anharmonicity and quantum fluctuations.

|	PBEsol	MLFF-PS	rSCAN	MLFF-rSCAN	HSE06	RPA	MLFF-RPA	Expt.
Cubic								
a (Å)	3.8934	3.8929	3.8988	3.8989	3.8931	3.9040	3.9040	3.900
$\Delta E_{\text{c-t}}$ (meV)	4.5	4.7	1.7	2.1	0.15	3.2	2.9	
ω_{FE} (meV)	8.4i	7.6i	10.4i	9.9i	15.8i	20.1i	17.4i	
ω_{AFD} (meV)	9.2i	9.5i	7.1i	7.9i	8.4i	8.1i	8.4i	
Tetragonal								
a (Å)	3.8848	3.8845	3.8934	3.8936	3.8910		3.8966	3.896
c/a	1.0050	1.0050 (1.0042)	1.0032	1.0030 (1.0021)	1.0013		1.0048 (1.0032)	1.001
V (Å^3)	58.92	58.91	59.21	59.20	58.99	59.48	59.45	59.19
θ_z (°)	5.0	5.0	3.9	3.9	2.7		4.4	2.1
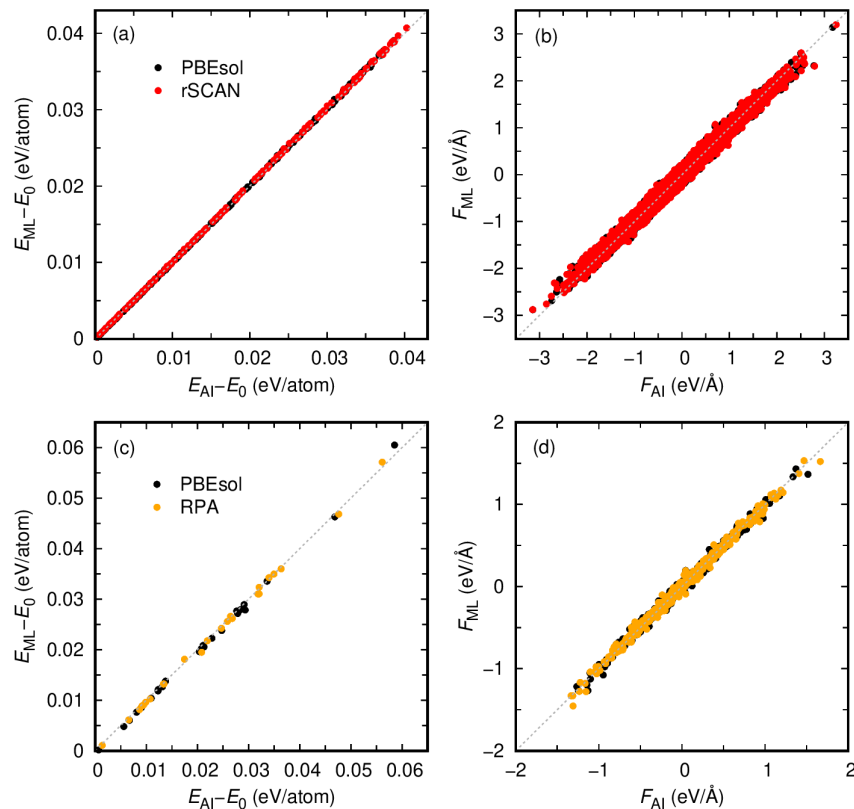
FIG. S3.   Comparison between the (a, c) energies and (b, d) forces for test datasets obtained directly from AI calculations and using the corresponding MLFFs. In (a) and (b) the AI calculations were performed using the PBEsol (black) and rSCAN (red) DFT functionals, while in (c) and (d) we considered PBEsol (black) and the RPA (orange) with a reduced test set. In (a) and (c) the energies are shifted to the minimum energy in each dataset E_0. The lines are a guide to the eye.
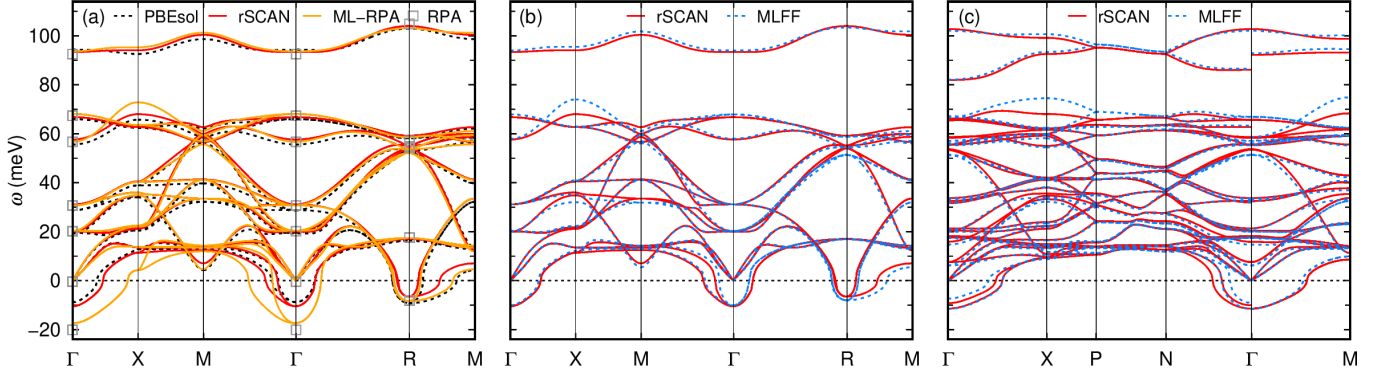
FIG. S4. (a) Phonon dispersions of cubic SrTiO$_3$ calculated using different functionals (PBEsol and rSCAN) and the RPA, including long-range dipole-dipole interactions. In the case of the RPA, the MLFF was used to compute the phonon dispersions along high-symmetry lines in the Brillouin zone. A direct RPA calculation was performed for a body-centered cubic cell containing 10 atoms, which yields the phonon frequencies at the Γ and R points of the simple cubic Brillouin zone. (b, c) Comparison between the AI phonon dispersions calculated using rSCAN and the corresponding MLFF results for (b) cubic and (c) tetragonal SrTiO$_3$. Negative values denote imaginary frequencies.
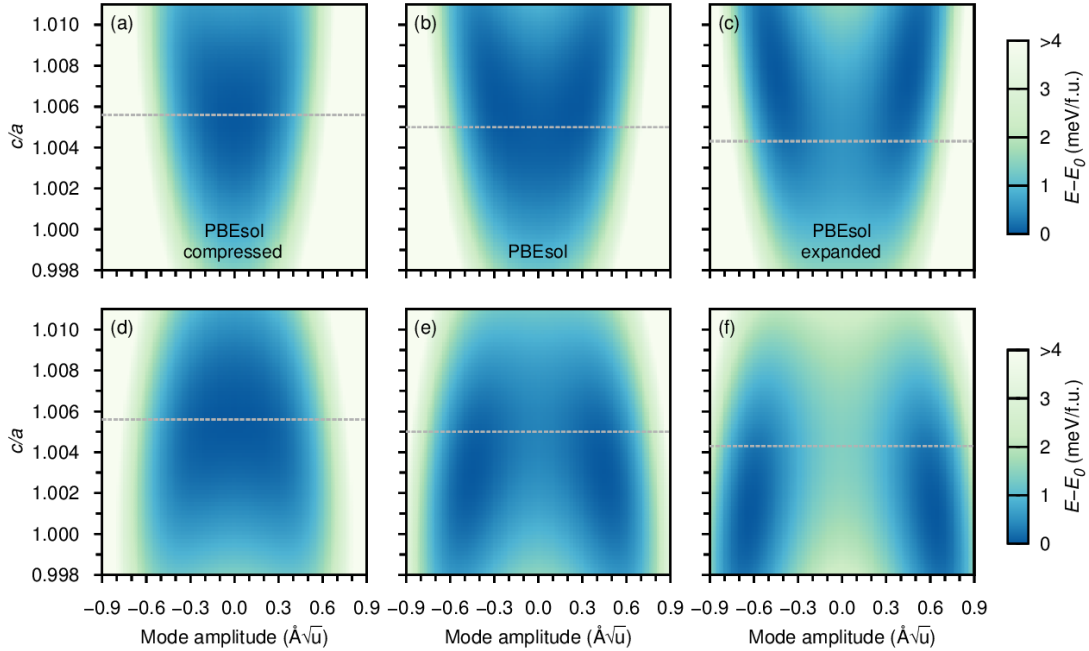
FIG. S5. 2D potential energy surfaces for tetragonal SrTiO$_3$ calculated at fixed volumes using the MLFF trained on PBEsol. Each point corresponds to a configuration where the atoms are displaced along a ferroelectric soft mode, and shear strain is applied to the unit cell. The mode amplitude and the c/a ratio are indicated on the x and y axis, respectively. In panels (a)-(c) the ferroelectric mode is the A_{2u} mode, and in panels (d)-(f) it is the doubly degenerate E_u mode. The volume in (b) and (e) is the equilibrium one. In (a) and (d) the volume is compressed by 0.75%, and in (c) and (f) it is expanded by 0.75%. The horizontal lines indicate the equilibrium value of c/a at each volume.
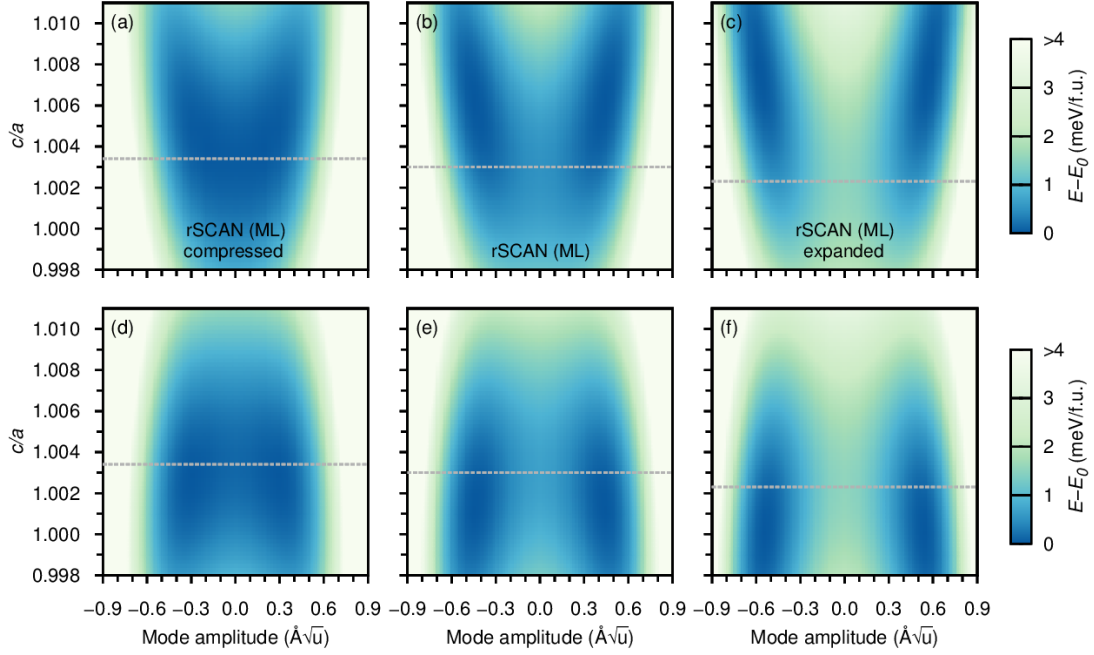
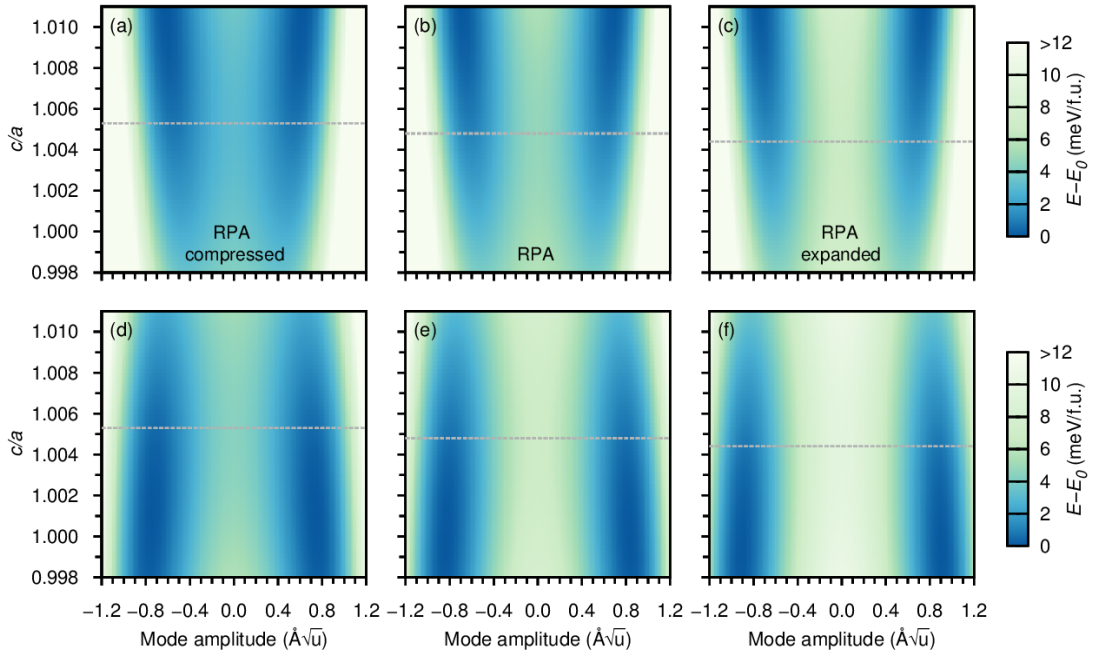FIG. S6.   Same as Fig. S5, but using the MLFF trained on rSCAN.

FIG. S7.   Same as Fig. S5, but using the MLFF trained on the RPA. Note the wider range of mode amplitudes on the x axis.
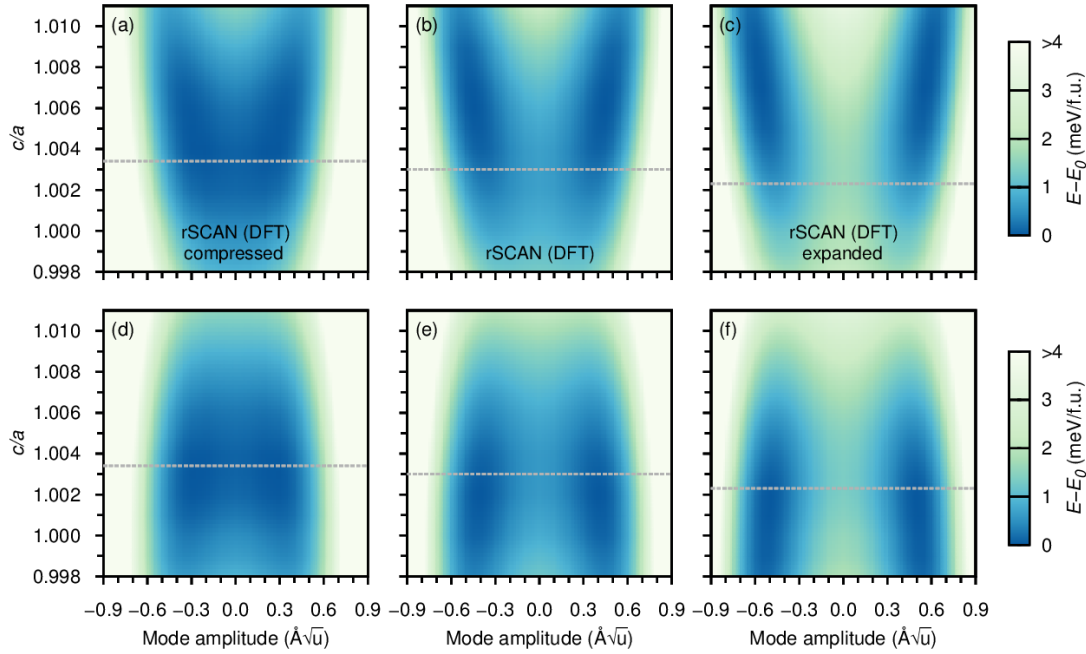
FIG. S8. Same as Fig. S5, this time obtained directly from DFT calculations using the rSCAN functional. The comparison with Fig. S6 confirms the accuracy of the MLFF trained on rSCAN. Similar calculations using PBEsol yield a comparison of the same quality with the MLFF results in Fig. S5.
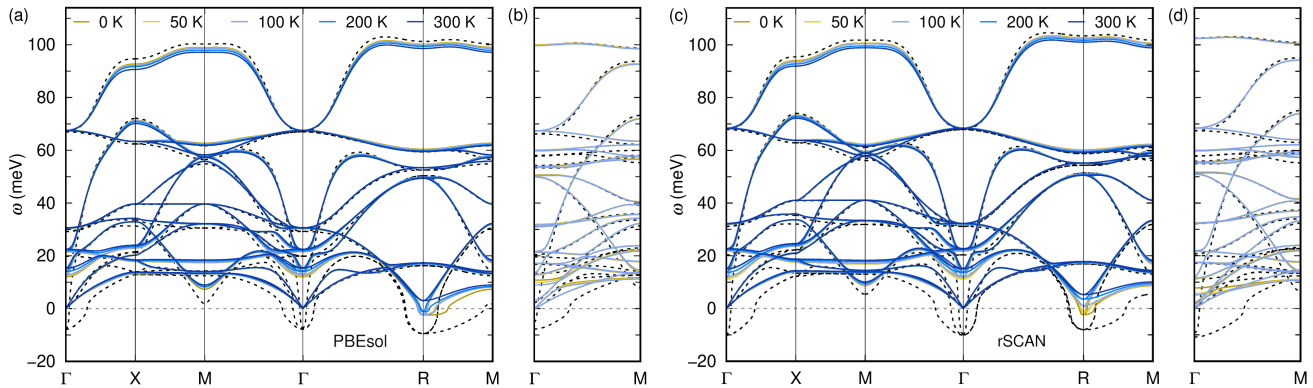

FIG. S9. Temperature-dependent phonon dispersions calculated using the SSCHA and the MLFF trained on (a, b) PBEsol and (c, d) rSCAN data. The volumes are the zero-temperature ones, with the c/a ratio minimizing the temperature-dependent anharmonic free energy. Panels (a) and (c) are for the cubic phase, and panels (b) and (d) for the tetragonal one (only the high-symmetry ΓM line in the Brillouin zone is shown for the latter). The harmonic results are shown as dashed lines. In (d), the light blue line corresponds to 75 K instead of 100 K.
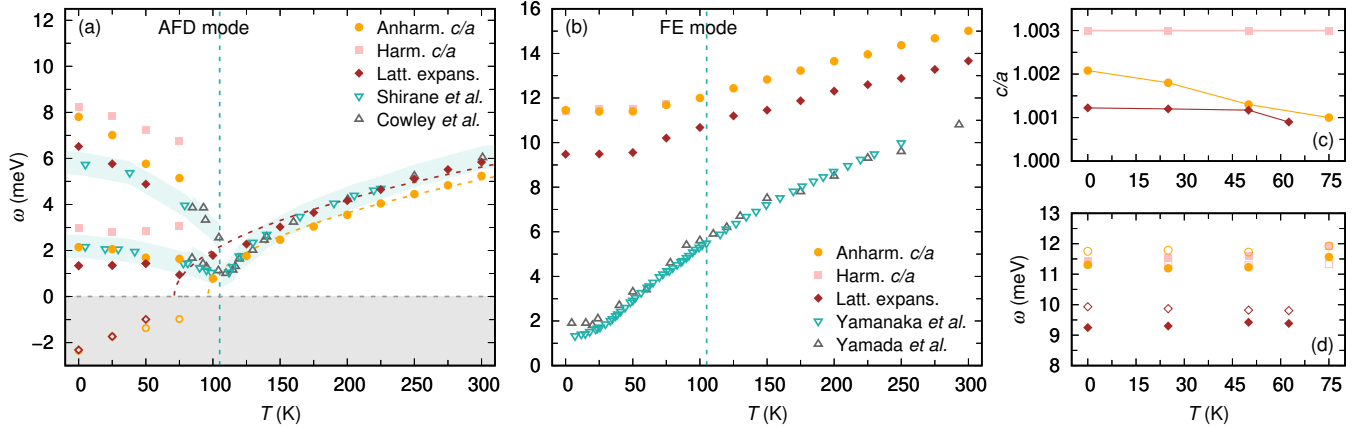
FIG. S10. Analysis of the effects of anharmonicity in the c lattice parameter elongation and lattice expansion within rSCAN. (a) AFD and (b) FE soft modes as a function of temperature. The orange circles are the same results reported in Fig. 3 in the main text, where the effects of anharmonicy on the lattice elongation (c/a ratio) are taken into account. The pink squares are obtained with c/a fixed to the harmonic 0 K value, with the effect of artificially flattening the temperature dependence of the A_{1g} and E_g energies, and the brown diamonds correspond to calculations allowing for the full anharmonic lattice expansion. We find a thermal expansion coefficient at room temperature of 2.46×10^{-5} K^{-1}, in excellent agreement with the one extracted from experimental data [20]. In this case, the AFD transition temperature is smaller (71 K) and the phonon energies slightly decrease. As in Fig. 3 in the main text, experimental measurements are also reported, and the dashed vertical lines indicate the experimental T_c. The empty symbols in the negative frequency region in (a) represent imaginary phonons obtained when the symmetry of the structure is kept cubic across the whole temperature range. (c) Equilibrium c/a ratio obtained at fixed volume (orange) and after taking into account volume expansion (brown). The pink data show the equilibrium harmonic value. (d) Close-up of the FE soft mode in the tetragonal phase showing the splitting into the A_{2u} (empty symbols) and E_u (filled symbols) branches. The colors have the same meaning as in panels (a)-(c). If the c/a ratio is fixed to the harmonic 0 K value, the sign of the splitting is the opposite. This conclusion holds also for RPA and PBEsol. Note that if only the c lattice parameter is allowed to fluctuate, while keeping the in-plane lattice vectors fixed, we find an elongated lattice and a softer A_{2u} frequency (not shown), in line with the results of Ref. [21]. However, this is akin to modelling epitaxially strained SrTiO$_3$ [22] rather than the equilibrium structure.
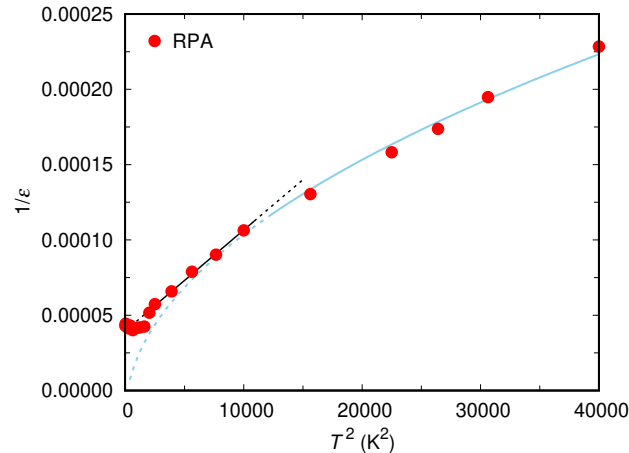

FIG. S11. Inverse of the dielectric function plotted against the square of the temperature up to 200 K. The dielectric function is estimated from the Lyddane-Sachs-Teller relation, assuming that the temperature dependence only comes from the soft phonon frequency (calculated from the RPA) and aligning the 0 K value to the experimental one [23]. As shown by the black (linear fit) and light blue (square-root fit) lines, the measured T^2 dependence of the inverse dielectric function at low temperatures is reproduced, followed by the linear T regime [24]. Our data do not capture the minuscule non-monotonic behavior of the dielectric function observed in Ref. [24], as this would require to resolve the temperature-dependent soft phonon frequencies with better than 0.1 meV accuracy.
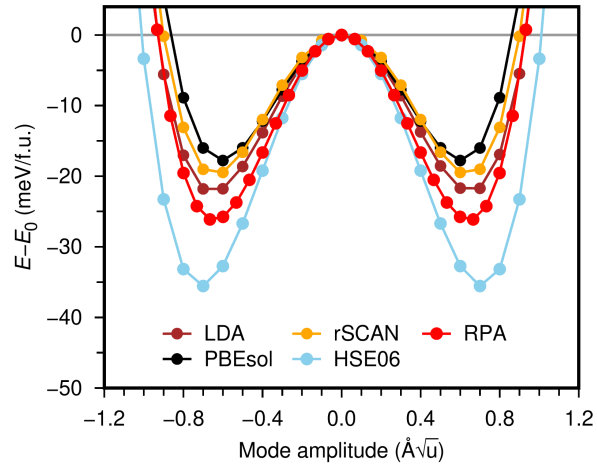
FIG. S12. Ferroelectric PES of BaTiO$_3$ calculated by displacing the atoms in the cubic phase along one of the FE modes. Results obtained using the LDA, PBEsol, rSCAN and HSE06 functionals are shown, as well as the RPA, all at the experimental lattice parameter. The well depth is related to the transition between the paraelectric cubic phase and the FE tetragonal one. As discussed in the main text, previous calculations predicted too low transition temperatures T_c. Neglecting quantum effects, a T_c of 275 K was obtained using the LDA (after applying a negative pressure to compensate for the underestimation of the lattice constant) [25], while using PBEsol T_c is about 182 K [26], as compared to the experimental value of 393 K. Note that quantum effects would *lower* the predicted T_c by about 30 K [25]. These results imply that the energy barrier for the transition is underestimated. Relating the computed transition temperatures to the calculated PES, our results indicate that the RPA would restore good agreement with the experiment, while HSE06 would yield a too large T_c.

* carla.verdi@univie.ac.at
† Present address: School of Physics, The University of Sydney, New South Wales, 2006, Australia

[1] G. Kresse and J. Hafner, Phys. Rev. B **47**, 558 (1993).
[2] G. Kresse and J. Furthmüller, Phys. Rev. B **54**, 11169 (1996).
[3] J. P. Perdew, A. Ruzsinszky, G. I. Csonka, O. A. Vydrov, G. E. Scuseria, L. A. Constantin, X. Zhou, and K. Burke, Phys. Rev. Lett. **100**, 136406 (2008).
[4] A. P. Bartók and J. R. Yates, J. Chem. Phys. **150**, 161101 (2019).
[5] J. Heyd, G. E. Scuseria, and M. Ernzerhof, J. Chem. Phys. **118**, 8207 (2003).
[6] A. V. Krukau, O. A. Vydrov, A. F. Izmaylov, and G. E. Scuseria, J. Chem. Phys. **125**, 224106 (2006).
[7] M. Kaltak, J. Klimeš, and G. Kresse, Phys. Rev. B **90**, 054115 (2014).
[8] J. Harl, L. Schimka, and G. Kresse, Phys. Rev. B **81**, 115126 (2010).
[9] R. Jinnouchi, F. Karsai, and G. Kresse, Phys. Rev. B **100**, 014105 (2019).
[10] R. Jinnouchi, F. Karsai, C. Verdi, R. Asahi, and G. Kresse, J. Chem. Phys. **152**, 234102 (2020).
[11] A. P. Bartók, M. C. Payne, R. Kondor, and G. Csányi, Phys. Rev. Lett. **104**, 136403 (2010).
[12] A. Tröster, C. Verdi, C. Dellago, I. Rychetsky, G. Kresse, and W. Schranz, Phys. Rev. Mater. **6**, 094408 (2022).
[13] P. Liu, C. Verdi, F. Karsai, and G. Kresse, Phys. Rev. B **105**, L060102 (2022).
[14] I. Errea, M. Calandra, and F. Mauri, Phys. Rev. Lett. **111**, 177002 (2013).
[15] L. Monacelli, R. Bianco, M. Cherubini, M. Calandra, I. Errea, and F. Mauri, J. Phys: Condens. Matter **33**, 363001 (2021).
[16] M. Zacharias, G. Volonakis, F. Giustino, and J. Even, Preprint at arxiv.org/abs/2209.12036.
[17] R. Bianco, I. Errea, L. Paulatto, M. Calandra, and F. Mauri, Phys. Rev. B **96**, 014111 (2017).
[18] U. Aseginolaza, R. Bianco, L. Monacelli, L. Paulatto, M. Calandra, F. Mauri, A. Bergara, and I. Errea, Phys. Rev. Lett. **122**, 075901 (2019).
[19] L. Cao, E. Sozontov, and J. Zegenhagen, Phys. Stat. Sol. A **181**, 387 (2000).
[20] A. Okazaki and M. Kawaminami, Mat. Res. Bull. **8**, 545 (1973).
[21] D. Shin, S. Latini, C. Schäfer, S. A. Sato, U. De Giovannini, H. Hübener, and A. Rubio, Phys. Rev. B **104**, L060103 (2021).
[22] J. H. Haeni, P. Irvin, W. Chang, R. Uecker, P. Reiche, Y. L. Li, S. Choudhury, W. Tian, M. E. Hawley, B. Craigo, A. K. Tagantsev, X. Q. Pan, S. K. Streiffer, L. Q. Chen, S. W. Kirchoefer, J. Levy, and D. G. Schlom, Nature **430**, 758 (2004).
[23] K. A. Müller and H. Burkard, Phys. Rev. B **19**, 3593 (1979).
[24] S. E. Rowley, L. J. Spalek, R. P. Smith, M. P. M. Dean, M. Itoh, J. F. Scott, G. G. Lonzarich, and S. S. Saxena, Nat. Phys. **10**, 367 (2014).
[25] J. Íñiguez and D. Vanderbilt, Phys. Rev. Lett. **89**, 115503 (2002).
[26] L. Gigli, M. Veit, M. Kotiuga, G. Pizzi, N. Marzari, and M. Ceriotti, npj Comput. Mater. **8**, 209 (2022).